Electronic Supporting Information

Progressive changes in crystallographic textures of biominerals generate functionally graded ceramics

*David Wallis, Joe Harris, Corinna F. Böhm, Di Wang, Pablo Zavattieri, Patrick Feldner, Benoit Merle, Vitaliy Pipich, Katrin Hurle, Lars N. Hansen, Frédéric Marin, and Stephan E. Wolf**

Experimental Details

Electron backscatter diffraction analysis: Orientation data were processed and plotted using Oxford Instruments HKLChannel5 software. Misindexed pixels with > 10° misorientation from each of their eight neighbors were removed, and unindexed pixels with at least six neighbors within the same prism were filled with the average orientation of their neighbors. Analysis of elastic properties, such as Young's modulus, was performed using the MTEX 4.5 toolbox for MATLAB®, following the approach of Mainprice *et al.* and using the elastic stiffness tensor for calcite of Chen *et al.*[54,55] This approach was preferred over common experimental techniques for quantifying variations in heterogeneous mechanical properties over micrometer length-scales, such as nanoindentation,[20] which also can measure an effective elastic modulus. However, for highly anisotropic materials such as calcite, which exhibits auxeticity,[85] it is not appropriate to use conventional equations based on isotropic elasticity to derive Young's modulus from effective indentation moduli, as they do not account for variation in Poisson's ratio.[20] The method that we employed to predict elastic properties is widely used and tested in the geological sciences,[54,86,87] and previous work suggests that the organic content of biogenic calcite prisms does not cause its elastic properties to deviate significantly from those of geological calcite.[20]

XRD and Anisotropic Scherrer Analyses: X-ray diffraction analysis was performed at a D8 diffractometer (Bruker AXS, Karlsruhe, Germany) equipped with a 9-fold sample changer. Specimens were prepared by a front-loading method in quadruplicate. The following measurement parameters were applied: range 10–90° 2θ; step size 0.011° 2θ, integration time 0.4 s; radiation: Cu K_α; generator

settings: 40 mA, 40 kV; divergence slit: 0.3°. Rietveld refinement was performed by means of the software TOPAS V5 (Bruker AXS, Karlsruhe, Germany. For the refinement of calcite, a hkl phase with the space group and lattice parameters of the calcite structure ICSD #80869 by Maslen et al.[88] was used to obtain an optimum fit. The lattice parameters a and c were refined. For the refinement of crystallite (coherent scattering domain) sizes, an anisotropic crystallinity model was applied, in which the shapes of the crystallites were simulated by suitable geometric models, following the approach of Ectors et al.[76]. A triaxial ellipsoid model was chosen and its dimension was defined by three radii *rx*, *ry*, and *rz*. The radius in *z*-direction, *rz*, is parallel to the crystallographic [*c*]-axis of the trigonal calcite crystallites, and rx is parallel to the [*a*]-axis. Due to the crystallographic requirements of the trigonal system *rx* and *ry* are equal.

Thermogravimetric analysis: Prisms were separated by bleaching, which disintegrated the interprismatic organics and the periostracum while keeping the mineral prisms intact. The prismatic shell layers were cut into small pieces, which were immersed in sodium hypochlorite solution (0.25 g of active chlorine/100 ml of water) for three days. After filtration, the prisms were collected by filtration and rinsed with water. Samples were powdered and subjected to thermogravimetry analysis under nitrogen atmosphere at a heating rate of 5 K min^{-1} (TA Instruments, TGA Q5000).

***Small and ultra-small angle neutron scattering (SANS, VSANS)*:** Small-Angle Neutron Scattering (SANS) experiments were performed on KWS-2 and KWS-3 instruments operated by Jülich Centre for Neutron Science (JCNS) at the Heinz Maier-Leibnitz Zentrum (MLZ) in Garching, Germany.[89,90] With the focusing SANS instrument KWS-3, scattering vectors *Q* from 0.0001 to 0.35 $Å^{-1}$ are accessible, at sample-to-detector distances of 9.2, 1.25, 0.25 and 0.05 m. This resolution was reached by a toroidal mirror with focus-to-focus distance 22 m, entrance aperture 2x2 mm^2, wavelength λ = 12.8 Å ($\Delta\lambda/\lambda$ = 17), and two-dimensional position-sensitive scintillation detector with diameter 9 cm and pixel size 0.32 mm. To improve scattering statistics above Q = 0.02 $Å^{-1}$ experiments were also carried out at the classical pinhole SANS instrument KWS-2 at sample-to-

detector distances of 2 and 8 m (corresponding collimation length of 4 and 8 m), and wavelength of λ = 5 Å ($\Delta\lambda/\lambda$ = 10%). Within the configurations mentioned above, KWS-2 covers a Q-range from 0.01 to 0.45 $Å^{-1}$. Powders of separated prisms were placed into a demountable quartz cell with a path length of 0.1 mm. The data reduction, analysis, background subtraction and fitting were performed using the software QtiKWS (V. Pipich, 2019, http://www.qtikws.de). A multi-level Beaucage fit was applied.[79]

Mechanical Testing: To determine hardness and fracture toughness of the prisms, nano- and microindentation studies were performed on transverse cross-sections of the prismatic layer. Prior to indentation the sections were polished using a Multiprep lapping unit (Allied technologies) with 0.5 µm diamond lapping films. The nanoindentation experiments were performed using a nanoindenter XP (Keysight Technologies Inc., USA) and a Berkovich diamond tip with a maximum penetration depth of 200 nm. The continuous stiffness measurement (CSM) technique, with a frequency of 45 Hz and a harmonic displacement amplitude of 2 nm, was applied to characterize the evolution of the hardness and effective elastic modulus as a function of penetration depth.[91–93] The measurements were started after reaching a stable thermal drift-rate less than 0.05 nm/s. To further account for thermal drift effects, the force was held constant at the end of the unloading step at 10 % of maximum load for 60 s and the displacement data were corrected based on the measured drift rate. Crack-initiation studies were undertaken on at least 12 stiff and 12 compliant prisms. Nanoindentation measurements were performed in a load-controlled manner up to a maximum force of 15 mN using a diamond Berkovich indenter tip. Pop-ins caused by crack initiation were defined as a burst in the load-displacement curve of greater than 3 nm based on analysis of indents from tests with and without pop-in events. After indentation, samples were investigated with a Dimension 3100 atomic force microscope (Bruker Corporation, USA) operating in contact mode. Standard silicon nitride contact tips were used with a nominal tip radius of 20 nm. Image acquisition was performed at a scan-rate of 0.5 Hz and a resolution of 512x512 pixels.

Vickers micro-indentation studies were performed on transverse cross-sections of *P. margaritifera* and *P. nobilis*, and geological calcite prepared using the same protocol as for

nanoindentation studies. Geological calcite single crystals were indented parallel to the [c]-axis. The crystallographic orientation of the prepared geological calcite sample surface was assessed using EBSD. Samples were indented using a Zwick 3212 indenter (Zwick GmbH, Ulm, Germany) with 1 kg loading with 10 seconds loading time. Samples were subsequently sputter coated with gold and imaged with secondary electrons in a scanning electron microscope. For fracture toughness determination from Vickers indents, cracks were classified as Palmqvist-cracks. Fracture toughness was then determined using Equation 1 (given below), under the assumption that the cracks are approximately elliptical, and that horizontal crack length is therefore also a proxy for vertical crack depth.

$$K_{\mathrm{IC}} = 0.032\, H\sqrt{a} \cdot \sqrt{\frac{E}{H}} \cdot \left(\frac{c}{a}\right)^{-\frac{3}{2}} \qquad (1)$$

Finite-Element Modelling: To predict the effect of the gradient in Young's Modulus within the prismatic layer of *P. margaritifera* on the toughness of the material, we constructed finite-element models (FEMs) of a long strip of material with a pre-existing crack loaded in Mode I (Figure S5A–B). This particular condition mimics the condition induced by the indenter when the crack tip is sufficiently far away from the indenter. We modelled four distributions of Young's Modulus indicated in Figure S5C: the graded distribution based on the EBSD-derived distribution in *P. margaritifera* (red line), the inverse graded distribution (blue line), a discrete layered distribution (green line), and a homogeneous distribution (black line). The finite-element computational domain is shown in Figure S5D. The length and width of the domain were 4.8 mm and 0.6 mm, respectively. For the layered material, the domain was divided into 6 regions of width w_0 = 0.1 mm with constant Young's modulus. The values of Young's modulus were 79.4 GPa, 91.0 GPa, 92.8 GPa, 88.3 GPa, 86.5 GPa, and 86.4 GPa. For each case, we considered finite-element meshes with seven crack sizes, a = 1 µm, 12 µm, 25 µm, 38 µm, 50 µm, 75 µm, 100 µm, 125 µm, and 150 µm. The FEM analysis was performed in the software package Abaqus and we employed 2D plane strain elements (i.e., element CPE4R). We applied a uniform displacement at the top boundary and symmetry boundary conditions at the bottom of the mesh. The mesh was refined at the crack tip, as displayed in Figure S5D. The

mesh size around the crack tip was determined by a preliminary convergence study on the values of the J-integral with three different mesh sizes, presented in Figure S5H. Thereby, the element size near the crack tip was determined to be small enough to provide an accurate stress field. To determine the stress intensity factor variation at the crack tip for the various cases, we employed a "modified" J-integral because the conventional J-integral method (also implemented and available in Abaqus) could be path-dependent for the heterogeneous case. Conversely, the modified J-integral is independent of the contour path that is chosen. Based on previous works,[94–99] we adopt the following J-Integral:

$$\bar{J} = \sum_{A}\sum_{p=1}^{N}\left\{\left[\sigma_{ij}u_{i,1}q_{1,j} - Wq_{1,1} - W_{,1}q_1\right]\det\frac{\partial x_k}{\partial \zeta_l}\right\}_p w_p \quad (1)$$

where, w_p are the weights of integration, det() is the determinant of Jacobian matrix, W is the strain energy density, $u_{i,1}$ is the derivative in the x-direction of the displacements, q_1 is a continuous function with value zero on the outer contour and value one on all the other contours except the outer path.[94–99] N is the number of integration points, A is the area of integration contour, and σ_{ij} is the components of the Cauchy stress tensor. We note also that $W_{,1} = \frac{dW}{dx} = \frac{dW}{dE(x)} \cdot \frac{dE(x)}{dx}$, E is a function of x, and $W = 0.5(\varepsilon_{11}\sigma_{11} + \varepsilon_{22}\sigma_{22} + \gamma_{12}\sigma_{12})$. Based on the constitutive law for plane strain, we can derive the equation of $\frac{dW}{dE(x)}$ using the chain rule:

$$q_{1,i} = \begin{Bmatrix}\frac{\partial q_1}{\partial x}\\ \frac{\partial q_1}{\partial y}\end{Bmatrix} = \begin{bmatrix}\frac{\partial x}{\partial \xi} & \frac{\partial y}{\partial \xi}\\ \frac{\partial x}{\partial \eta} & \frac{\partial y}{\partial \eta}\end{bmatrix}^{-1}\begin{Bmatrix}\frac{\partial q_1}{\partial \xi}\\ \frac{\partial q_1}{\partial \eta}\end{Bmatrix} \quad (2)$$

where ξ and η are orthogonal axes of the standard quadrilateral element, $q_1 = N_m Q_m$, N is the shape function of each element, and Q is the scalar value 1 or 0. Finally, we use equation (3) to calculate stress intensity factor K_{I}.

$$K_{\mathrm{I}} = \sqrt{\frac{\bar{J}\cdot E_{\mathrm{tip}}}{1-\upsilon^2}} \quad (3)$$

While the conventional J-integral is expected to be path-dependent, previous works [10-11] have demonstrated that under very specific conditions (e.g., for very small contours within refined mesh close to the crack tip), the modified and conventional J-integral can give the same results. A comparison between the modified and conventional J-integrals is presented in Fig. S5E for graded material and in Fig. S5F for inverse graded material. The values of the modified and conventional J integral close to the crack tip for both materials are equal. Modified J integral values are independent of contours of elements. One element contour includes ring elements around the crack tip, presented in Fig. S5D. As expected, the conventional J-integral begins to give different results for larger contours. A close-up plot of the normal stress distribution along the thickness of the strip of material is presented in Fig. S5G. Normalized stress intensity factors of heterogenous materials $K^*_{\mathrm{I},het}$ were calculated on the basis of equation (4), where $K_{\mathrm{I},hom}$ is the non-normalized stress intensity factor of the homogeneous material and $K_{\mathrm{I},het}$ that of the heterogeneous material.

$$K^*_{\mathrm{I},het} = \frac{K_{\mathrm{I},hom} - K_{\mathrm{I},het}}{K_{\mathrm{I},hom}} \quad (4)$$

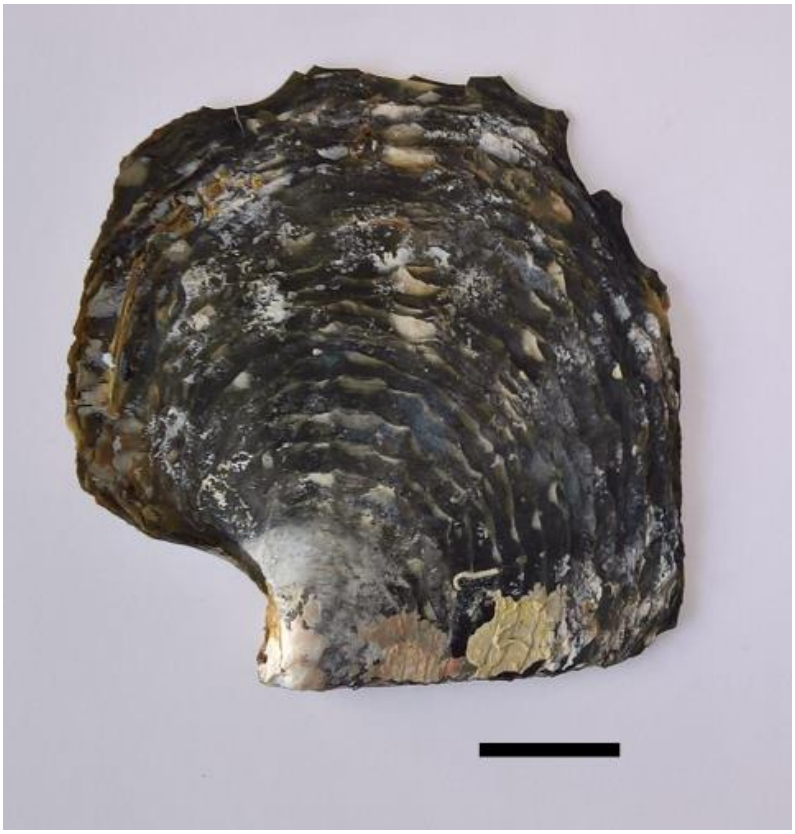

Figure S1. Macrophotograph of *Pinctada margeritifera*. Scale bar: 4 cm.

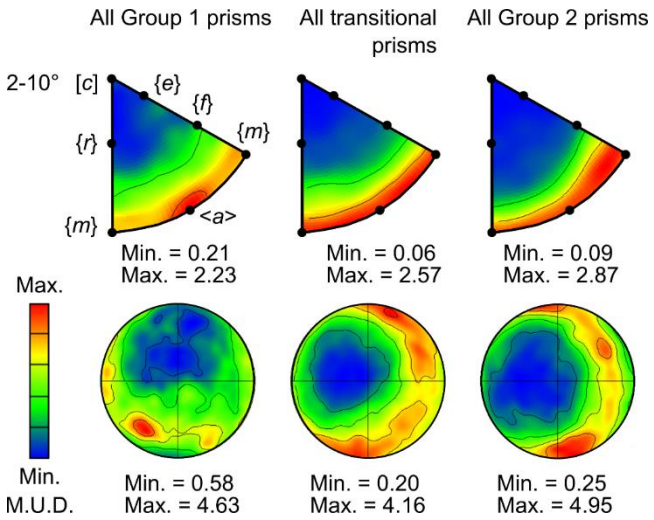

Figure S2. Axes of 2–10° lattice rotations within Group 1, transitional, and Group 2 prisms.

Plots are presented in both the crystal (top) and sample (bottom, lower-hemisphere) reference frames. In all groups, rotation axes are approximately perpendicular to the [*c*]-axis and exhibit some bias towards <*a*>-axes in Group 1, consistent with dispersions of crystal axes in pole figures in Figure 2. Rotation axes in Group 1 prisms are predominantly oblique to both the growth direction and the plane of the shell, whereas those in Group 2 prisms are predominantly parallel to the growth direction. Contours are multiples of uniform distribution (M.U.D.).

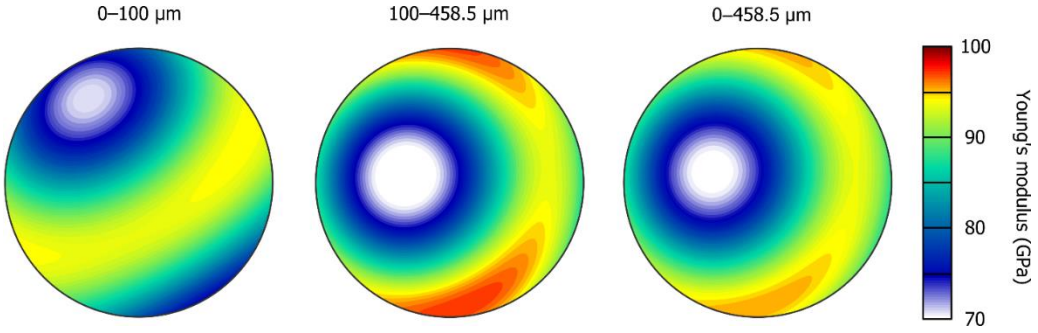

Figure S3. Anisotropy in Young's modulus

Stereoplots of Young's modulus for different portions of the prismatic layer, calculated from the Hill average of the Voigt and Reuss bounds on the elastic stiffness tensor[54,86]. Distances correspond to the Y-axis in Figure 1. All distributions are highly anisotropic. In the outer 100 µm of the prismatic layer, the maximum Young's modulus is oriented approximately 60° oblique to the surface normal of the shell, yielding a Young's modulus of ~80 GPa perpendicular to the shell surface. In the remainder of the prismatic layer, the maximum Young's modulus aligns with and remains parallel with the surface normal of the shell, yielding a Young's modulus of ~95 GPa.

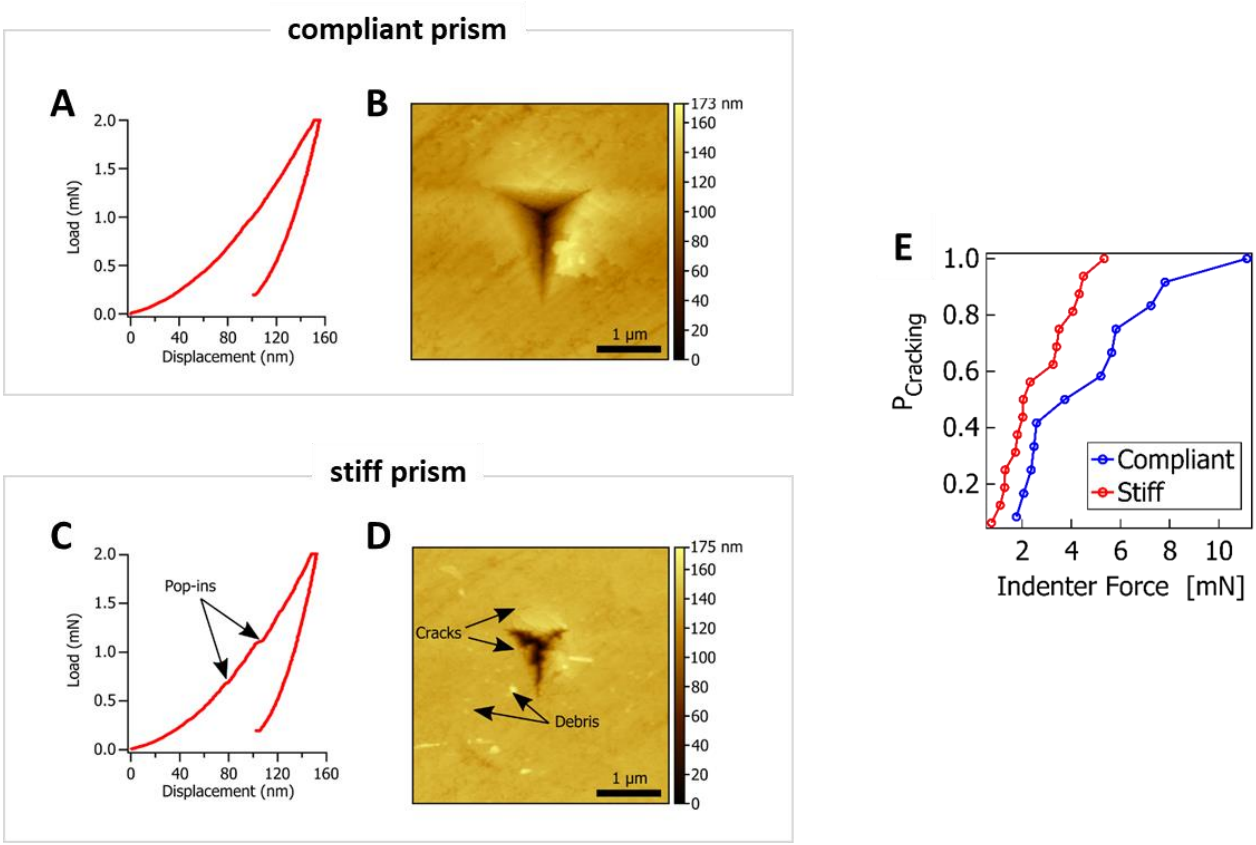

Figure S4. Nanoindentation analysis of compliant and stiff prisms of *P. margaritifera*.
(A) Load-displacement curve recorded from a test on a compliant prism close to the shell exterior; no pop-ins are visible. **(B)** AFM image of the indent corresponding to the load-displacement curve in A; no cracks are visible. **(C)** Load-displacement curve recorded from a test on a stiff prism close to the shell interior; pop-ins are clearly visible. **(D)** AFM image of the indent corresponding to the load-displacement curve in C. Multiple cracks are present at the edges of the indent and surface debris is present due to cracking. (**E)** Probability of crack initiation as a function of load for stiff and compliant prisms measured using nanoindentation.

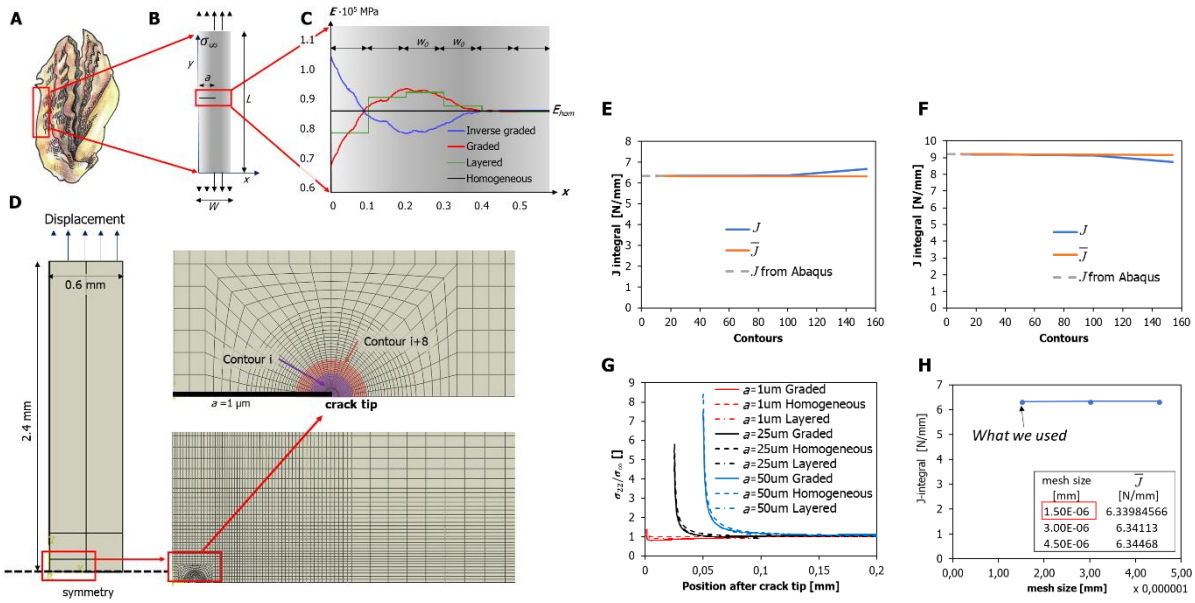

Figure S5. Details on the finite-element modelling.
(A, B) FEM model description. Original locus of the material strip and crack tip subjected to uniaxial stress conditions imposing a Mode I loading condition at the pre-existing crack. **(C)** Young's modulus distributions considered in the model: graded, inverse graded, layered, and homogeneous distributions. **(D)** Mesh details with loading and boundary conditions (example shown with a crack size a = 1 µm). **(E)** Comparison of conventional integral calculation on J-integral values (blue) and "modified" J-integral calculation for graded materials (orange), coupled with the domain integral prediction from ABAQUS. **(F)** Comparison of domain integral calculation on J-integral values (blue) and modified J-integral calculation for inverse graded materials (orange), coupled with the domain integral prediction from ABAQUS. **(G)** Normalized opening stress distribution close to crack tip for three different sizes of crack model. **(H)** Mesh convergence study on model with crack size a=50 µm.

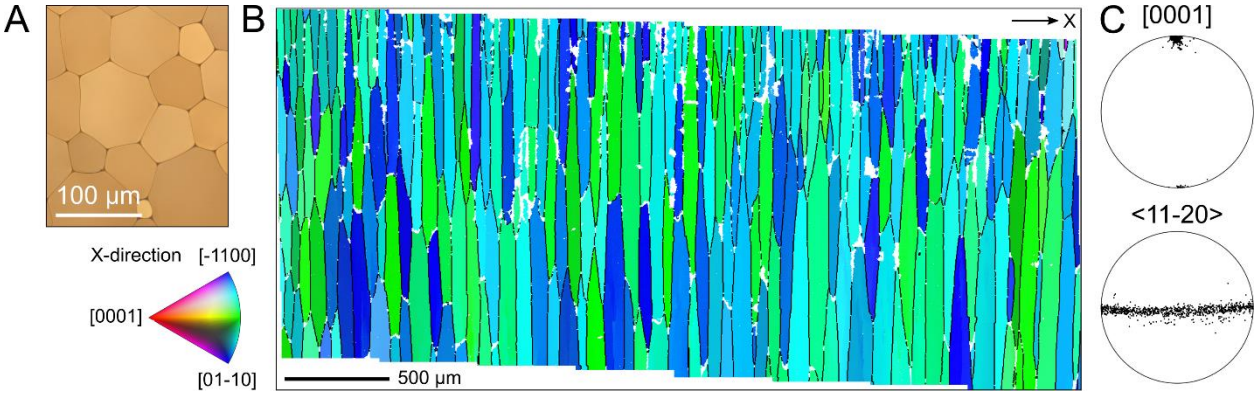

Figure S6. The prismatic layer of *Pinna nobilis*

(A) Reflected light micrograph of a transverse section exhibiting tessellating polygonal prisms. **(B)** Electron backscatter diffraction map of a longitudinal section colour-coded by the inverse pole figure for the crystal direction aligned with the X-axis. No orientation gradients within prisms or systematically across the layer are evident. **(C)** Pole figures of the c[0001] and a<11-20> axes of the prisms in B. [0001] axes are aligned parallel to the growth direction and <11-20> axes are parallel to the plane of the shell.

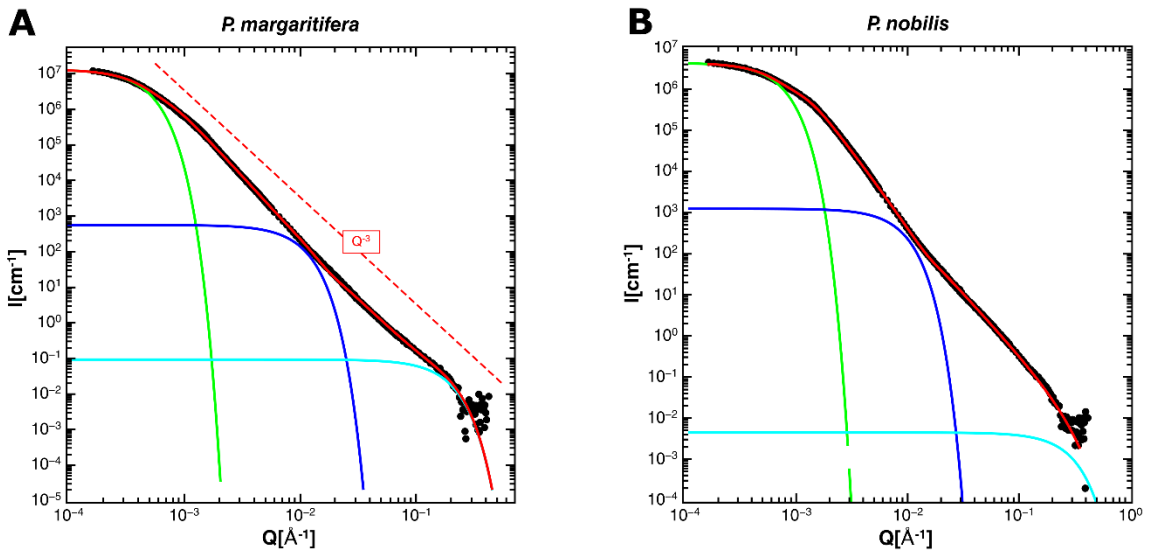

Figure S7. Small and very-small angle neutron scattering on powdered prisms extracted from both nacroprismatic bivalves.

The experimental data is given by full circles. The prisms of both bivalves, *P. margaritifera* and *P. nobilis* are both characterized as a mass fractal with a Porod exponent of 3. A red dotted line gives a Q^{-3} as a visual guide. Full colored lines give the respective fit based on a multi-level Beaucage form factor model. The calcite prisms of *P. nobilis* are composed of three different units characterized by a radius of gyration of 275 ± 7 nm, 22.5 ± 0.5 nm, and 0.7± 0.01 nm, respectively. In the case of *P. margaritifera*, again, three structural units are found, with similar characteristic gyration radii of 435 ± 10 nm, 20.4 ± 1 nm, and 1.11 ± 0.03 nm.